Research Square

Preprints are preliminary reports that have not undergone peer review.
They should not be considered conclusive, used to inform clinical practice,
or referenced by the media as validated information.

Adsorption of Rhodamine B onto Natural Zeolite: Mechanistic Insights, Response Surface Optimization, and Comparative Machine Learning Prediction

WuZhen Yan
Universiti Sains Malaysia
Rosnani Alkarimiah
cerosnani@usm.my
Universiti Sains Malaysia

Research Article

Keywords: Adsorption, Machine learning, Mordenite, Natural zeolite, Response surface methodology, Rhodamine B, SHAP analysis

Posted Date: November 25th, 2026

DOI: https://doi.org/10.21203/rs.3.rs-11606322/v1

License: This work is licensed under a Creative Commons Attribution 4.0 International License.
Read Full License

Additional Declarations: No competing interests reported.

Adsorption of Rhodamine B onto Natural Zeolite: Mechanistic Insights, Response Surface Optimization, and Comparative Machine Learning Prediction

WuZhen Yan, Rosnani Alkarimiah*

School of Civil Engineering, Universiti Sains Malaysia, Engineering Campus, 14300 Nibong Tebal, Penang, Malaysia

First author.

WuZhen Yan, Environmental Engineering Programme, School of Civil Engineering, Universiti Sains Malaysia, Engineering Campus, 14300 Nibong Tebal, Penang, Malaysia.

E-mail: yan.wuzhen20011008@student.usm.my

ORCID: 0009-0002-3102-0453

*** Corresponding author.**

Rosnani Alkarimiah, Environmental Engineering Programme, School of Civil Engineering, Universiti Sains Malaysia, Engineering Campus, 14300 Nibong Tebal, Penang, Malaysia.

E-mail: cerosnani@usm.my

ORCID: 0000-0002-8821-4614

Submitted to: *BMC Chemistry*

Article type: Research article

Date of submission: 3 November 2026

Abstract

Rhodamine B (RhB) was adsorbed onto an unmodified natural zeolite, and the removal was modeled by response surface methodology (RSM) and by machine learning (ML). X-ray diffraction showed that the zeolite phase is mordenite, with quartz as the main accompanying mineral. Energy-dispersive X-ray spectroscopy gave a mean Si/Al ratio of 5.58, and the Brunauer-Emmett-Teller surface area was 26.6 m^2/g. The adsorption kinetics followed the pseudo-second-order model (R^2 = 0.980), and equilibrium was reached within 90 min. Among the single-factor experiments, solution pH had the strongest influence: removal decreased from 98.0% at pH 2 to 49.0% at pH 6, as RhB changes from its cationic to its zwitterionic form across its pK_a of 3.7. The Langmuir isotherm gave the best fit (R^2 = 0.991), with a maximum monolayer capacity of 6.60 mg/g at pH 6. A quadratic RSM model fitted to a three-factor, three-level full factorial design (30 runs) described the data well (R^2 = 0.967, predicted R^2 = 0.911, $p < 0.0001$). Support vector regression (SVR), random forest, and extreme gradient boosting were trained on the same dataset and evaluated by leave-one-out cross-validation (LOOCV). SVR gave the highest LOOCV R^2 (0.925), but nested LOOCV, which removes the optimistic bias of hyperparameter tuning, lowered it to 0.858, below the value of the RSM model. Shapley additive explanations (SHAP) gave the same feature ranking for all three ML models, and this ranking matched the analysis of variance. On this small designed-experiment dataset, the quadratic model predicted as well as the best ML model, and ML served mainly as an interpretive check.

Keywords: *Adsorption; Machine learning; Mordenite; Natural zeolite; Response surface methodology; Rhodamine B; SHAP analysis*

1. Introduction

Synthetic dyes are extensively used in the textile, printing, paper, leather, and food industries, with an estimated 10–15% of the total production discharged into aquatic environments during manufacturing and processing operations. [1,2] These colored effluents block light and inhibit photosynthesis in receiving waters, and many dyes or their degradation products are toxic, mutagenic, or carcinogenic. [3] Among cationic dyes, Rhodamine B (RhB; $C_{28}H_{31}ClN_2O_3$, molar mass 479.02 g/mol) is a water-soluble xanthene dye widely employed as a biological stain, fluorescent tracer, and textile colorant. RhB is chemically stable and resistant to conventional biological treatment, and its persistence in treated effluents has motivated the development of dedicated removal techniques. [1,3,4]

Adsorption is widely used for dye-laden wastewater because it is simple to operate, inexpensive to install, effective at low concentrations, and not inhibited by toxic pollutants. [2,5,6] Activated carbon is still the benchmark adsorbent, but it is costly and hard to regenerate, so cheaper materials such as agricultural wastes, clay minerals, and zeolites have been studied as alternatives. [5,6] Natural zeolites are hydrated aluminosilicate minerals whose three-dimensional framework carries a net negative charge arising from isomorphous substitution of Si^{4+} by Al^{3+}; this charge is balanced by exchangeable cations (Na^+, K^+, Ca^{2+}, Mg^{2+}) residing in the structural channels and cavities. [7,8] Clinoptilolite, the most abundant natural zeolite, has a cation exchange capacity (CEC) of 1.5–2.2 meq/g and has been used to remove ammonium, heavy metals, and some organic pollutants from water. [7,9–11] Although numerous studies have reported the adsorption of cationic dyes onto modified zeolites (e.g., surfactant- or acid-modified forms), comparatively few investigations have addressed the use of unmodified natural zeolite for bulky xanthene dyes such as RhB, and the underlying adsorption mechanism remains incompletely characterized. [12–16] In particular, because RhB is larger than the channel apertures of common natural zeolites such as clinoptilolite and mordenite, the nature of the accessible sites and the relative contributions of ion exchange and non-electrostatic interactions on the external surface remain unresolved, and the capacity values reported for unmodified natural zeolite have not been accompanied by a designed-experiment evaluation of the combined effects of pH, dosage, and initial concentration.

Response surface methodology (RSM) is the standard statistical framework for the multifactor optimization of adsorption processes, providing a second-order polynomial description of the response and of the factor interactions from a small designed set of experiments. [17,18] Because the quadratic form may not capture strongly nonlinear response surfaces, [19] machine learning (ML) algorithms such as random forest (RF), [20] support vector regression (SVR), [21] and extreme gradient boosting (XGBoost) [22] have increasingly been applied as complementary predictive tools in environmental science and engineering, [23,24] and comparisons of ML with RSM on adsorption data have reported improved accuracy in some systems but not in others. [25–29] The SHAP (SHapley Additive exPlanations) framework [30] further allows the contribution of each input variable to the individual ML predictions to be quantified, so that the patterns learned by a model can be checked against the experimental trends. However, most comparisons of ML with RSM have evaluated ML performance using random train/test splits or resubstitution metrics, without isolating the optimistic bias that arises when hyperparameters are selected on the same cross-validation predictions used to score the model. On the small designed-experiment datasets typical of adsorption RSM studies, this practice can systematically favor flexible learners over the fixed-form polynomial. Whether the reported superiority of ML persists under bias-corrected evaluation has received little attention.

Both questions are examined here for the adsorption of RhB onto an unmodified natural zeolite. The work had four objectives. The first was to characterize the adsorbent by X-ray diffraction, N_2 physisorption, scanning electron microscopy, and infrared spectroscopy, and to establish the adsorption mechanism from batch experiments (kinetics, dosage, pH, and isotherm studies). The second was to quantify the combined effects of pH, dosage, and initial concentration and to identify favorable operating conditions with a three-factor, three-level full factorial design and RSM. The third was to train RF, SVR, and XGBoost models on the same 30-run dataset and to compare their predictive performance with that of the RSM model under leave-one-out cross-validation. The fourth was to use SHAP analysis to check whether the feature importance rankings and response patterns learned by the ML models agree with the analysis of variance and with the trends found in the batch experiments.

2. Materials and Methods

2.1. Materials and reagents

Natural zeolite powder (particle size < 75 μm) was procured from Henan Yixin Minerals Co., Ltd. (Henan, China). Its mineral phases were identified by X-ray diffraction (Section 3.1). The zeolite was used as received without any chemical or thermal pretreatment. Rhodamine B (dye content ≥ 95%) was purchased from Sigma-Aldrich. A stock solution of 100 mg/L RhB was prepared by dissolving the appropriate mass in deionized water and stored in amber glass bottles to prevent photodegradation. Working solutions of the desired concentrations were obtained by dilution of the stock solution. Solution pH was adjusted using 0.1 mol/L HCl and 0.1 mol/L NaOH. All chemicals were of analytical reagent grade, and deionized water was used throughout.

2.2. Adsorbent characterization

The mineral phase composition of the natural zeolite was determined by X-ray diffraction (XRD) on a Rigaku MiniFlex 600 diffractometer operated at 40 kV and 15 mA with Cu Kα radiation (λ = 1.5406 Å), over a 2θ range of 3–90° with a step size of 0.01° and a scan rate of 2°/min. The specific surface area and pore characteristics were measured by N_2 adsorption-desorption at 77 K on a CIQTEK physisorption analyzer; the sample was degassed at 200 °C for 4 h prior to analysis. The surface area was calculated by the Brunauer-Emmett-Teller (BET) method, the external surface area and the micropore volume by the *t*-plot method, and the mesopore size distribution by the Barrett-Joyner-Halenda (BJH) method. Surface morphology and elemental composition were examined by scanning electron microscopy (SEM) coupled with energy-dispersive X-ray spectroscopy (EDX) on a Thermo Scientific Axia ChemiSEM after sputter coating with gold; images were acquired at an accelerating voltage of 5 kV and EDX spectra at 15 kV. Fourier transform infrared (FTIR) spectra were recorded over 4000–500 cm^{-1} at a resolution of 4 cm^{-1} with 16 scans per spectrum. XRD, N_2 physisorption, and SEM-EDX were performed on the raw zeolite. FTIR spectra were collected for both the raw zeolite and the RhB-loaded zeolite (obtained by adsorption at pH 2, followed by filtration and drying at ≤ 60 °C) for comparison.

2.3. Batch adsorption experiments

All batch adsorption experiments were conducted using a jar test apparatus (six-paddle stirrer) at a stirring speed of 150 rpm and a working volume of 500 mL at ambient temperature (25 ± 2 °C). At predetermined time intervals, aliquots were withdrawn and filtered through 0.45 μm membrane filters prior to spectrophotometric analysis. The residual RhB concentration was determined at 554 nm using a UV-Vis spectrophotometer (Hach DR3900). A calibration curve was established over 0–2.5 mg/L ($A = 0.2641C + 0.0028$, where A is the absorbance at 554 nm measured in a 1 cm quartz cell and C the RhB concentration in mg/L; $R^2 > 0.999$), covering the photometric range in which the Beer-Lambert response remains linear. Samples whose absorbance exceeded the linear range were diluted with deionized water before measurement. All pH values quoted in this work refer to the initial pH setpoint, adjusted prior to adsorbent addition. Each single-factor experiment (kinetics, dosage, pH, and isotherm) was conducted in duplicate, and the reported values are the means of the duplicates. The data of these experiments are provided in Tables S1–S4 of the Supplementary Material (Additional file 1). The equilibrium adsorption capacity and the removal efficiency were calculated using Eqs. (1) and (2), respectively:

$$q_e = (C_0 - C_e)V/m \quad (1)$$

$$\text{Removal (\%)} = [(C_0 - C_e)/C_0] \times 100 \quad (2)$$

where q_e (mg/g) is the equilibrium adsorption capacity, C_0 and C_e (mg/L) are the initial and equilibrium RhB concentrations, respectively, V (L) is the volume of solution, and m (g) is the mass of adsorbent.

2.3.1. Adsorption kinetics

Kinetic experiments were carried out at a zeolite dosage of 2 g/L, an initial RhB concentration of 10 mg/L, and an initial pH of 6. Samples were collected at 0, 5, 15, 30, 60, 90, and 120 min. The experimental data were fitted to the pseudo-first-order (PFO) model, [31] the pseudo-second-order (PSO) model, [32] and the Weber-Morris intraparticle diffusion model [33] using nonlinear regression (Eqs. (3)–(5)):

$$q_t = q_e[1 - \exp(-k_1 t)] \quad (3)$$

$$q_t = k_2 q_e^2 t/(1 + k_2 q_e t) \quad (4)$$

$$q_t = k_{id} t^{0.5} + C \quad (5)$$

where q_t (mg/g) is the amount adsorbed at time t (min), k_1 (min^{-1}) and k_2 (g/(mg·min)) are the pseudo-first-order and pseudo-second-order rate constants, respectively, k_{id} (mg/(g·$min^{0.5}$)) is the intraparticle diffusion rate constant, and C (mg/g) is a constant proportional to the boundary-layer thickness (reported as C_1 and C_2 for the two successive diffusion stages in Table 1).

2.3.2. Effect of adsorbent dosage

The effect of adsorbent dosage on RhB removal was investigated at dosages of 2, 4, 5, 6, and 8 g/L, with an initial RhB concentration of 10 mg/L, pH 6, and a contact time of 90 min.

2.3.3. Effect of solution pH

The effect of initial solution pH was examined at pH 2, 4, 6, 8, 10, and 12, with a zeolite dosage of 2 g/L, an initial RhB concentration of 10 mg/L, and a contact time of 90 min. The initial pH was adjusted using 0.1 mol/L HCl or NaOH prior to adsorbent addition.

2.3.4. Adsorption isotherms

Isotherm experiments were performed at initial RhB concentrations of 5, 10, 20, 30, 50, 75, and 100 mg/L, with a zeolite dosage of 2 g/L, pH 6, and a contact time of 120 min (exceeding the kinetic equilibrium time of 90 min). The equilibrium data were fitted to the Langmuir, [34] Freundlich, [35] and Sips [36] isotherm models by nonlinear regression (Eqs. (6)–(8)):

$$q_e = q_{max} K_L C_e/(1 + K_L C_e) \quad (6)$$

$$q_e = K_F C_e^{1/n} \quad (7)$$

$$q_e = q_{max}(K_S C_e)^{m_S}/[1 + (K_S C_e)^{m_S}] \quad (8)$$

where q_{max} (mg/g) is the maximum monolayer adsorption capacity, K_L (L/mg) is the Langmuir affinity constant, K_F ((mg/g)(L/mg)$^{1/n}$) and $1/n$ are the Freundlich capacity and heterogeneity constants, K_S (L/mg) is the Sips affinity constant, and m_S (dimensionless) is the Sips heterogeneity exponent.

2.4. Experimental design and RSM

A three-factor, three-level full factorial design was employed to investigate the combined effects of initial solution pH (*A*: 2, 4, 6), adsorbent dosage (*B*: 2, 5, 8 g/L), and initial RhB concentration (*C*: 10, 30, 50 mg/L) on the equilibrium residual concentration (C_e, mg/L), selected as the response to avoid ceiling effects at high removal. The design consisted of $3^3 = 27$ factorial points plus three center-point replicates (pH 4, 5 g/L, 30 mg/L), giving 30 runs executed in random order under the conditions of Section 2.3 (150 rpm, 25 ± 2 °C, 500 mL, 90 min), with center points interspersed among the factorial runs. Run 14 coincides with the center-point combination, providing four replicate observations (Runs 14 and 28–30) for the pure-error estimate with 3 degrees of freedom. A full factorial design was preferred over the Box-Behnken design because it samples the factor space uniformly and provides the same observations to both the polynomial and ML models, so that the two approaches are compared on identical data. [17,37]

The factors were coded as $A = (\text{pH} - 4)/2$, $B = (\text{dosage} - 5)/3$, and $C = (C_0 - 30)/20$, and a second-order polynomial in the coded variables was fitted by ordinary least squares. Model adequacy was evaluated by analysis of variance (ANOVA) with Type III sums of squares, including the *F* test for overall significance, the lack-of-fit test, R^2, adjusted R^2 (adj-R^2), predicted R^2 (pred-R^2), and adequate precision. Response surface and contour plots were generated from the fitted model, and the conditions minimizing C_e were identified within the coded design space $[-1, +1]^3$ by multi-start L-BFGS-B optimization. The RSM analysis was performed in Python 3.11 with NumPy 2.4 and SciPy 1.17.

2.5. Machine learning modeling

Three ML algorithms, random forest (RF), [20] support vector regression (SVR) with a radial basis function kernel, [21] and extreme gradient boosting (XGBoost), [22] were trained on the same 30-run dataset to predict C_e from pH, dosage, and C_0. Hyperparameters were selected by exhaustive grid search (Additional file 1: Table S5) using the R^2 of the aggregated leave-one-out cross-validation (LOOCV) predictions as the selection criterion; in LOOCV each of the 30 observations is held out in turn while the remaining 29 serve as the training set, so that every observation is used once as the test point and no random partition is involved. [38,39] Input features for SVR were standardized to zero mean and unit

variance with the scaler fitted on the training portion of each fold only, whereas RF and XGBoost were trained on the raw feature values, because tree splits are invariant to feature scaling. For the quadratic RSM model the LOOCV predictions were obtained from the prediction error sum of squares (PRESS) residuals through the hat-matrix diagonal, which is algebraically equivalent to refitting on the training portion of every fold for a linear model. Predictive performance was quantified by R^2, root mean square error (RMSE), and mean absolute error (MAE) of the held-out predictions, and the training R^2 of each model fitted to all 30 runs was recorded to indicate the degree of overfitting. Differences between two models were tested on the paired absolute LOOCV residuals with the two-sided exact Wilcoxon signed-rank test. Because selecting hyperparameters on the same LOOCV predictions used to score the model gives an optimistic estimate, [40,41] a nested LOOCV was additionally run for SVR. In each of the 30 outer folds, the grid search was repeated within the 29 training observations, and the configuration selected by the inner loop was refitted to predict the held-out observation, so that the test point contributed neither to model fitting nor to hyperparameter selection. All stochastic models were initialized with random_state = 42.

To interpret the ML predictions, SHAP analysis [30] was performed on the models trained on the full dataset, using TreeExplainer for RF and XGBoost and KernelExplainer for SVR, the latter with the 30 standardized training samples as the background dataset, nsamples = 500 per instance, the identity link function, and a fixed sampling seed (42). For a common feature space, the three models used for the SHAP analysis were fitted on the standardized features, which does not alter the tree models. All ML computations were performed in Python 3.11 using scikit-learn 1.8, XGBoost 3.2, and SHAP 0.51.

3. Results and Discussion

3.1. Characterization of the natural zeolite

The XRD pattern of the natural zeolite is shown in Fig. 1a. Peak positions are given as measured, and the *d*-spacings quoted below were calculated with the quartz reflections as an internal reference. The peaks at 2θ = 6.64°, 9.88°, 13.57°, 19.77°, 22.38°, and 25.74° can be indexed as the (110), (200), (111), (330), (150), and (202) reflections of mordenite, an orthorhombic zeolite of the MOR framework type,

[42] and further mordenite lines appear at 27.88° and 30.98°. The strongest line of the pattern (26.75°) and the lines at 21.03°, 36.65°, 39.58°, 42.64°, 50.22°, 60.02°, and 68.45° belong to quartz. Weaker reflections of mordenite and quartz are also marked in Fig. 1a. The remaining weak features, among them a broad maximum near 6° (*d* of about 15 Å), a line at 9.04° (*d* of about 9.9 Å), and a few very sharp lines, the strongest at 30.39°, are attributed to minor layer silicates and other accessory phases. The reflection at 6.64° corresponds to a spacing of 13.5 Å, which matches the (110) plane of mordenite and exceeds the largest spacing allowed by the *C*2/*m* unit cell of clinoptilolite, [10] and the clinoptilolite (200) reflection expected near 11.2° has less than 3% of the height of the peak at 9.88°. The zeolite fraction of the material is therefore predominantly mordenite, with quartz as the main accompanying mineral; the co-occurrence of mordenite and quartz has also been reported for an Australian natural zeolite. [13] All structural arguments in the following sections are based on the mordenite framework.

EDX point analyses at two locations gave Al:Si atomic proportions of 15.4:84.6 and 15.0:85.0, corresponding to Si/Al ratios of 5.49 and 5.67 (mean 5.58). This value lies within the range of about 4.0 to 6.1 reported for natural mordenite, [43] whose ideal composition $Na_8[Al_8Si_{40}O_{96}]\cdot 24H_2O$ has a Si/Al ratio of 5.0. [42] Na, K, Ca, Mg, and Fe were also detected in the EDX spectra; Na, K, and Ca are the dominant extraframework cations of natural mordenite. [43] SEM images (Fig. 1b) show irregular, angular particles and aggregates ranging from below 1 μm to several tens of micrometers. At higher magnification the particle surfaces are rough and built of fine platy and needle-like crystallites with voids between them.

The N_2 adsorption-desorption isotherm is shown in Fig. 1c. In terms of the IUPAC classification, [44] it is a composite of types I and II with an H4 hysteresis loop, a combination typical of aggregated zeolite crystals. The appreciable uptake at $p/p° < 0.1$ reflects micropore filling, and the steep rise close to saturation, which does not reach a plateau, reflects condensation in the voids between crystallites and particles. The desorption branch closes steeply onto the adsorption branch between $p/p° = 0.50$ and 0.46, and below this pressure the two branches run close together without fully merging, which is often observed for microporous solids in which N_2 equilibrates slowly. The BET surface area, evaluated over $p/p° = 0.06–0.30$, is 26.6 m^2/g. The *t*-plot gives an external surface area of 8.81 m^2/g and a micropore volume of 0.0094 cm^3/g, and the total pore volume at $p/p° = 0.95$ is 0.0272 cm^3/g. The BJH analysis of

the adsorption branch shows that about 80% of the pore volume between 1.7 and 300 nm lies in pores wider than about 13 nm, in line with the voids between crystallites seen by SEM, and its cumulative surface area of 7.8 m^2/g is comparable to the *t*-plot external surface area. Similarly small surface areas have been reported for unmodified natural clinoptilolite and mordenite. [45] These values indicate that most of the channel system is not accessible to N_2, presumably because the channels are partly blocked by exchangeable cations and impurities. The external surface area, which refers to the bulk material and comprises the mesopore walls and the outer surface of the particles, is the quantity relevant to RhB uptake and is used in Section 3.6.

The FTIR spectra of the raw and RhB-loaded zeolite are compared in Fig. 1d. The broad band at 1047 cm^{-1} is assigned to the asymmetric T–O stretching vibration (T = Si or Al) of the aluminosilicate framework, [11,45] and the broad band at 3442 cm^{-1} to the O–H stretching vibration of zeolitic and adsorbed water, whose H–O–H bending vibration contributes to the broad absorption between about 1580 and 1640 cm^{-1}. The sharp features at 1632, 1384, and 1350 cm^{-1} appear at the same positions and with the same shapes in both spectra and are therefore unrelated to the dye. After RhB adsorption, the framework band remains within 3 cm^{-1} of its original position, that is, within the spectral resolution of 4 cm^{-1}, so the uptake of the dye leaves the aluminosilicate framework unchanged. No new band appears, as expected for a dye loading of at most 1.4 wt% (13.60 mg/g).

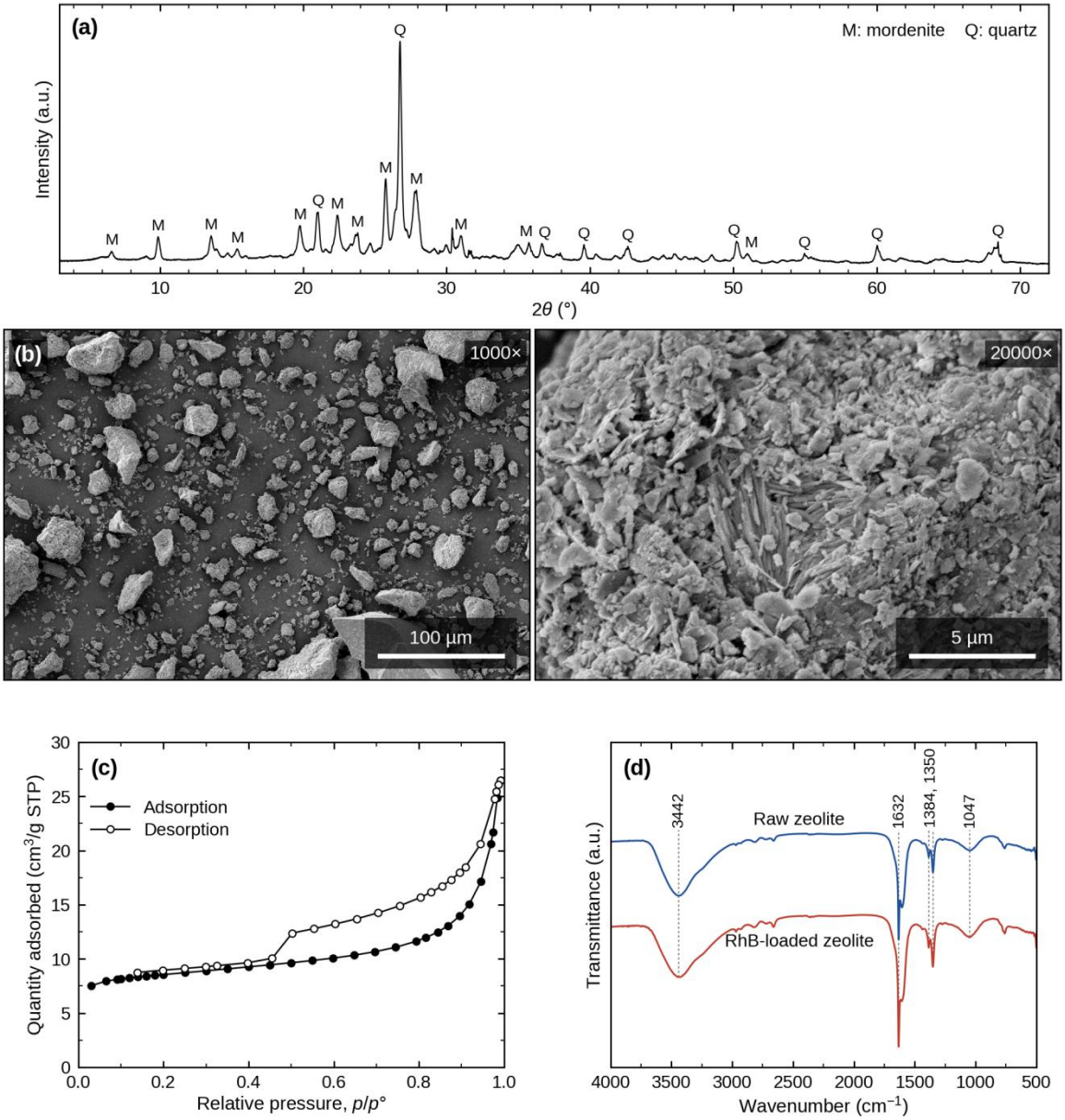

Fig. 1 Characterization of the natural zeolite: (a) XRD pattern between $2\theta = 3°$ and 72° (M, mordenite; Q, quartz), (b) SEM images at 1000× and 20000×, (c) N_2 adsorption-desorption isotherm at 77 K (STP, standard temperature and pressure), and (d) FTIR spectra of the raw and RhB-loaded zeolite, offset vertically for clarity

3.2. Adsorption kinetics

The kinetic profile of RhB adsorption onto natural zeolite is presented in Fig. 2a and Table 1. A rapid initial uptake was observed during the first 5 min of contact, with 33.0% of RhB removed, corresponding to an uptake of 1.65 mg/g. The rate of adsorption then decreased gradually, and removal

reached 49.1% (q_t = 2.46 mg/g) at 90 min and 49.9% (q_t = 2.50 mg/g) at 120 min. The increase in q_t of less than 2% between 90 and 120 min confirmed that adsorption equilibrium was effectively attained by 90 min; this time was therefore adopted as the contact time for the dosage, pH, and factorial experiments.

The pseudo-second-order (PSO) model provided a substantially better description of the experimental data (R^2 = 0.980) than the pseudo-first-order (PFO) model (R^2 = 0.942), with the PSO-predicted equilibrium capacity (q_e = 2.48 mg/g) in close agreement with the experimental value (2.50 mg/g at 120 min), whereas the PFO model underestimated it (q_e = 2.30 mg/g; Table 1). The better fit of the PSO model is taken here as an empirical description of the rate data and not as evidence of chemisorption. [46]

The Weber-Morris intraparticle diffusion plot (q_t versus $t^{0.5}$) exhibited two distinct linear segments (Table 1). The first segment (5–30 min) had the steeper slope (k_{id1} = 0.148 mg/(g·min$^{0.5}$)), reflecting rapid boundary-layer diffusion and external mass transfer, whereas the second segment (30–120 min) showed a reduced slope (k_{id2} = 0.067 mg/(g·min$^{0.5}$)), consistent with slower diffusion within the mesopores and the interparticle voids. The nonzero intercepts (C_1 = 1.30, C_2 = 1.81 mg/g) indicate that intraparticle diffusion was involved but was not the sole rate-controlling step. [33]

Table 1 Kinetic and isotherm model parameters for RhB adsorption onto natural zeolite

Model	Parameter	Value	Unit
PFO	q_e	2.30	mg/g
	k_1	0.213	min^{-1}
	R^2	0.942	–
PSO	q_e	2.48	mg/g
	k_2	0.125	g/(mg·min)
	R^2	0.980	–
Weber-Morris	k_{id1}	0.148	$mg/(g \cdot min^{0.5})$
	C_1	1.30	mg/g
	R^2 (stage 1)	0.972	–
	k_{id2}	0.067	$mg/(g \cdot min^{0.5})$
	C_2	1.81	mg/g
	R^2 (stage 2)	0.904	–
Langmuir	q_{max}	6.60	mg/g
	K_L	0.120	L/mg
	R^2	0.991	–
Freundlich	K_F	1.63	$(mg/g)(L/mg)^{1/n}$
	$1/n$	0.311	–
	R^2	0.935	–
Sips	q_{max}	6.77	mg/g
	K_S	0.113	L/mg
	m_S	0.940	–
	R^2	0.991	–

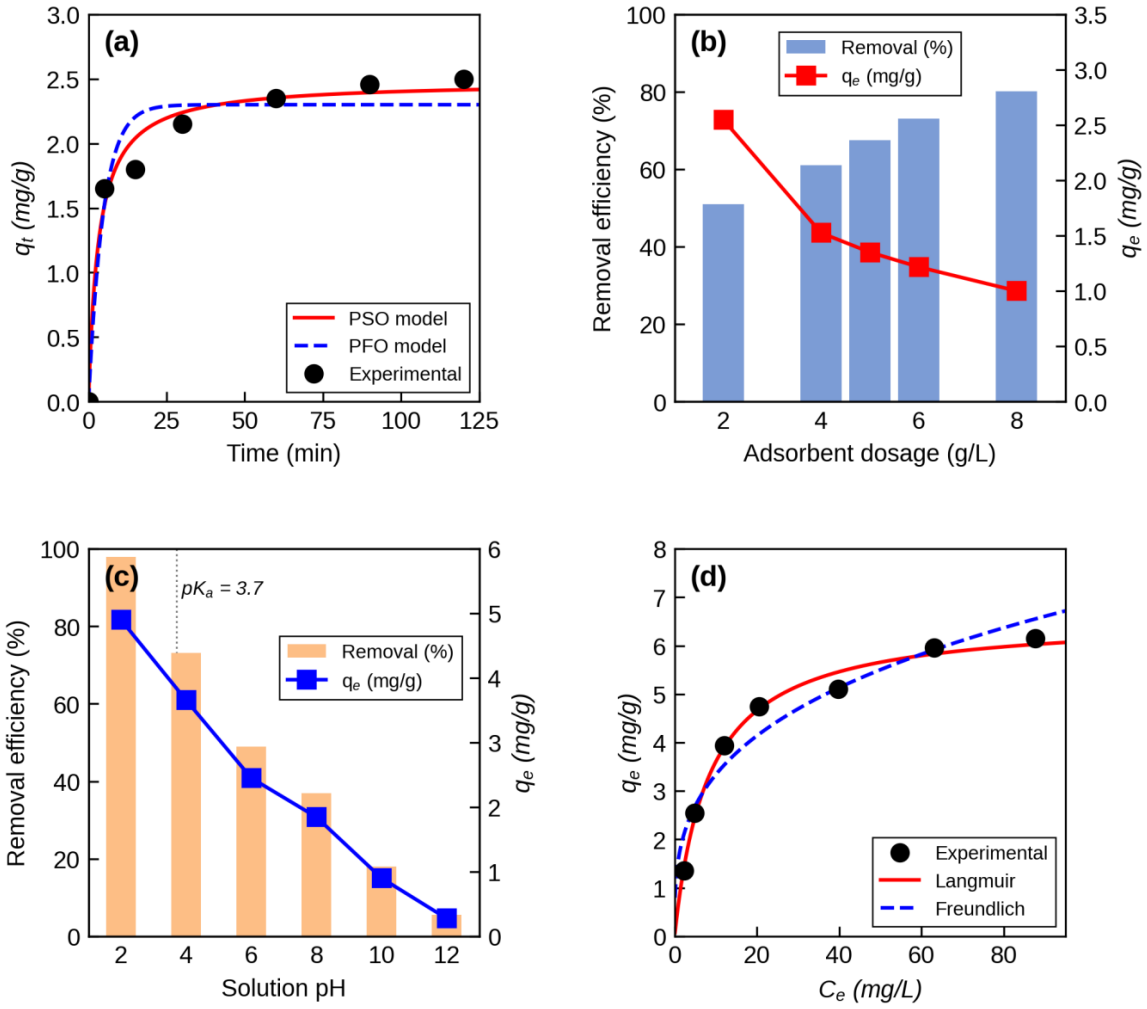

Fig. 2 Batch adsorption results: (a) kinetic profile with PFO and PSO model fits, (b) effect of adsorbent dosage on removal efficiency and adsorption capacity, (c) effect of solution pH with pK_a = 3.7 indicated, and (d) equilibrium isotherms with Langmuir and Freundlich model fits (pH 6, 25 °C); the Sips fit (Table 1) is visually indistinguishable from the Langmuir curve (maximum difference 0.07 mg/g) and is omitted for clarity

3.3. Effect of adsorbent dosage

Raising the zeolite dosage from 2 to 8 g/L increased the removal from 50.9% to 80.1% because more sites were available (Fig. 2b). The uptake per gram fell from 2.55 to 1.00 mg/g over the same range, as is usual when a fixed amount of dye is shared among more sites. [5,6] A dosage of 2 g/L was used for the kinetic, pH, and isotherm studies because it leaves measurable equilibrium concentrations over the whole concentration range.

3.4. Effect of solution pH

Solution pH exerted the most pronounced effect on RhB removal (Fig. 2c). The removal efficiency decreased sharply from 98.0% at pH 2 to 73.1% at pH 4, 49.0% at pH 6, 36.9% at pH 8, 18.0% at pH 10, and only 5.5% at pH 12. The corresponding adsorption capacity dropped from 4.90 mg/g at pH 2 to 0.27 mg/g at pH 12. This strong pH dependence indicates a dominant electrostatic contribution to the adsorption mechanism.

Rhodamine B (pK_a = 3.7) exists predominantly as a cationic species (RhB^+) at pH < 3.7, where the carboxyl group is protonated and the positive charge resides on the delocalized iminium moiety of the xanthene chromophore. [47] Above pH 3.7, the zwitterionic form predominates as the carboxyl group deprotonates, substantially reducing the net positive charge and hence the electrostatic driving force for interaction with negatively charged surfaces. The steep decline in removal from pH 2 to pH 6 follows this change in speciation.

Removal is still 73.1% at pH 4 and 49.0% at pH 6, where the zwitterionic form of RhB predominates, and this needs an explanation. According to the Henderson-Hasselbalch equation, approximately 33% of the RhB molecules remain in the cationic form at pH 4, and preferential uptake of the cationic fraction may shift the solution speciation equilibrium toward further protonation (Le Chatelier's principle), sustaining adsorption. At pH 6, the cationic fraction is negligible (approximately 0.5%), yet 49.0% removal is still observed. This residual uptake may be attributed to the localized positive charge density at the diethylamino groups of zwitterionic RhB, which retains some electrostatic affinity for the negatively charged zeolite surface, although less than the fully cationic form has. Hydrogen bonding between the carboxylate group of zwitterionic RhB and surface hydroxyl groups is another possible contribution at near-neutral pH.

The negative framework charge of mordenite is structural and does not depend on solution pH. The electrokinetic behavior of natural zeolites is best documented for clinoptilolite, whose framework charge has the same origin. Systematic measurements by Ersoy and Çelik [48] demonstrated that natural clinoptilolite carries a negative zeta potential across the entire pH 2–12 range with no isoelectric point, the potential shifting from approximately −18 mV at pH 2 to −40 mV at pH 12, and comparable behavior has been reported for natural zeolite and clinoptilolite in subsequent electrokinetic studies. [49,50]

Consequently, the zeolite surface can be expected to remain negatively charged under all conditions tested, providing a persistent electrostatic attraction for cationic RhB^+ at low pH values.

3.5. Adsorption isotherms

The equilibrium adsorption data at pH 6 are presented in Fig. 2d and Table 1. The Langmuir isotherm provided the best fit to the experimental data (R^2 = 0.991), yielding a maximum monolayer capacity of q_{max} = 6.60 mg/g and an affinity constant of K_L = 0.120 L/mg, whereas the Freundlich model gave a poorer fit (R^2 = 0.935), with K_F = 1.63 (mg/g)(L/mg)$^{1/n}$ and a heterogeneity parameter of $1/n$ = 0.311, a value between 0 and 1 that indicates favorable adsorption. [51] The Sips isotherm, of which the Langmuir model is the special case m_S = 1, yielded q_{max} = 6.77 mg/g and m_S = 0.940 ± 0.133; because the two models are nested, they were compared by the extra-sum-of-squares F test, and the additional Sips parameter did not produce a statistically resolvable improvement ($F(1, 4) = 0.19$, $p = 0.68$), so the more parsimonious Langmuir description was adopted. Given the pH dependence (Section 3.4) and the exclusion of RhB from the channels (Section 3.6), the Langmuir behavior is consistent with adsorption on a fairly uniform set of external-surface sites. The Langmuir maximum capacity is compared with those of other adsorbents in Table 2. The present capacity of the unmodified natural zeolite (6.60 mg/g at pH 6) lies within the range reported for comparable unmodified materials: 2.70 mg/g for chalcedonite, 4.25 mg/g for halloysite, 6.87 mg/g for rice husk silica, and 6.96 mg/g for a clinoptilolite-dominant natural zeolite. [52,53] Capacities of this order are what the limited external-surface site density of such materials affords. The higher values in Table 2 were obtained with chemically modified or synthetic adsorbents.

Table 2 Comparison of the RhB adsorption capacity of the natural zeolite with those of other adsorbents

Adsorbent	q_{max} (mg/g)	pH	T (°C)	Ref.
Natural zeolite (mordenite with quartz, this study)	6.60	6	25	–
Natural zeolite (clinoptilolite-dominant)	6.96	4.6	25	[52]
Halloysite	4.25	4.6	25	[52]
Chalcedonite	2.70	4.6	25	[52]
Rice husk-derived silica	6.87	7.05	27	[53]
Acid/CTAB-modified natural zeolite	7.96	7	30	[54]
SDS-modified Fe_2O_3/zeolite 13X	89.3	3	25	[55]
ZSM-5 synthesized from kaolin	128.21	7	n.r.	[56]
Banana peel (acid-treated)	9.52	2	28	[57]
Kaolin–organic bentonite composite	12.68	9.1	25	[58]
Sewage sludge biochar (HCl-activated)	16.94	n.r.	25	[59]
H_2SO_4-modified coal fly ash	36.36	4	30	[60]

The q_{max} values should be compared with caution, because pH, temperature, adsorbent dosage, and concentration range differ between studies. n.r. = not reported. CTAB = cetyltrimethylammonium bromide; SDS = sodium dodecyl sulfate.

3.6. Adsorption mechanism

The pH dependence (Section 3.4), the Langmuir capacity (Section 3.5), and the framework structure of mordenite together constrain the adsorption mechanism. The RhB molecule has approximate dimensions of 1.6 × 1.2 × 0.6 nm, whereas the main channels of mordenite, bounded by 12-membered rings, measure 0.65 × 0.70 nm, and the 8-membered ring channels only 0.26 × 0.57 nm. [42] Because two of the three dimensions of RhB exceed the width of the largest channel, the dye cannot enter the zeolite channels. Adsorption on the zeolite must therefore occur on the external surface and at channel mouth sites. The Langmuir maximum capacity is consistent with this picture: q_{max} = 6.60 mg/g corresponds to 13.8 μmol/g or approximately 0.014 meq/g, which is only about 0.6% of the theoretical CEC of 2.29 meq/g calculated from the ideal mordenite composition. [42] A more direct measure is the surface density of the adsorbed dye. On the basis of the *t*-plot external surface area of 8.81 m^2/g (Section 3.1), q_{max} corresponds to 0.94 molecules/nm^2, or 1.06 nm^2 per molecule, which is close to the footprint of an RhB molecule adsorbed edge-on (1.6 nm × 0.6 nm = 0.96 nm^2) and about half that of a molecule lying flat (1.6 nm × 1.2 nm = 1.92 nm^2). The Langmuir capacity at pH 6 is therefore on the order of one molecular layer on the external surface. The highest capacity observed in this study (13.60 mg/g at pH 2, 2 g/L, and C_0 = 50 mg/L; Run 3 in Table 3, Section 3.7) corresponds to 1.94 molecules/nm^2, or 0.52 nm^2 per molecule. This is more than a single layer can accommodate in any orientation, since even a

molecule standing upright on its smallest face would occupy 1.2 nm × 0.6 nm = 0.72 nm^2. Uptake under strongly acidic conditions thus exceeds a single layer on the surface probed by N_2. It may involve more than one layer or the adsorption of dye aggregates such as dimers, which RhB is known to form in aqueous solution. [47]

The pH-dependent removal, the speciation of RhB, the permanently negative framework charge, and the size exclusion therefore support an external-surface adsorption mechanism in which ion exchange of the cationic form is the principal pH-sensitive contribution: at low pH, cationic RhB^+ displaces native exchangeable cations (Na^+, K^+, Ca^{2+}) on the negatively charged external surface of the zeolite. Two observations indicate that this exchange is not purely coulombic. At an initial pH of 2, the proton concentration of 10 mmol/L exceeds the RhB concentration of 21 μmol/L by a factor of about 480, yet 98.0% removal is still observed. The selectivity for RhB^+ over H^+ is therefore well above that expected for a purely electrostatic exchange of monovalent ions. This points to a substantial non-coulombic contribution, such as hydrophobic and dispersion interactions and the entropy of dehydration, which is characteristic of large organic cations on aluminosilicate surfaces. In addition, removal continues to decline between pH 6 and pH 12, from 49.0% to 5.5%, over a range in which the speciation of RhB is essentially constant and the zeta potential reported for clinoptilolite (Section 3.4) becomes more, not less, negative. The concentration of the counter-cation introduced with the NaOH used for pH adjustment rises by several orders of magnitude over the same interval, so competitive exchange is a plausible contributor to this branch.

The two contributions can be separated quantitatively using the factorial data of Table 3 (Section 3.7). The uptake can be written as $q = q_{zwitt} + (q_{cat} - q_{zwitt})f_{cat}$, where f_{cat} is the cationic fraction given by the Henderson-Hasselbalch equation. With q_{cat} and q_{zwitt} calibrated on the pH 2 and pH 6 runs at 2 g/L, the model predicts the pH 4 uptake at C_0 = 50 mg/L as 9.11 mg/g against a measured 9.41 mg/g, and at C_0 = 30 mg/L as 8.33 mg/g against a measured 8.06 mg/g, that is, to within 3.4% at both concentrations with only two adjustable quantities. On this decomposition the pH-sensitive, exchange-attributable component amounts to roughly half of the uptake at pH 2, the remainder persisting into the zwitterionic regime. The decomposition applies where uptake is limited by the sites and not by the dye. At C_0 = 10

mg/L and pH 2, removal already reaches 96.9%, so q is set by the amount of dye available, not by the number of sites.

3.7. Response surface optimization

The single-factor experiments show how removal responds to each variable separately. The full factorial design adds the interactions and puts all three factors into one dataset.

3.7.1. ANOVA and model diagnostics

The full factorial design matrix and measured equilibrium concentrations are presented in Table 3. The coded-variable second-order polynomial for the residual concentration is:

$$C_e = 6.69 + 5.45A - 5.01B + 8.56C - 0.62AB + 3.93AC - 4.63BC - 1.02A^2 + 1.91B^2 + 2.81C^2 \quad (9)$$

where A, B, and C denote the coded values of pH, adsorbent dosage, and initial concentration defined in Section 2.4.

The ANOVA results are summarized in Table 4. The model was highly significant ($F = 65.38$, $p < 0.0001$) with $R^2 = 0.967$, adj-$R^2 = 0.952$, and pred-$R^2 = 0.911$; the difference of 0.041 between adj-R^2 and pred-R^2 is well within the recommended limit of 0.20, and the adequate precision of 32.18 far exceeds the minimum of 4, so the signal is large relative to the noise.

All three main effects were highly significant ($p < 0.0001$): initial concentration C_0 ($F = 272.89$, $\eta^2 = 0.449$) exerted the largest effect on C_e, followed by pH ($F = 110.72$, $\eta^2 = 0.182$) and dosage ($F = 93.26$, $\eta^2 = 0.153$). The pH × C_0 ($F = 38.36$) and dosage × C_0 ($F = 53.25$) interactions were highly significant ($p < 0.0001$), whereas the pH × dosage interaction was not ($F = 0.94$, $p = 0.34$), indicating that the effects of pH and dosage on the residual concentration are modulated by the initial concentration level, as expected for saturation-dependent adsorption. The B^2 ($F = 5.19$, $p = 0.034$) and C^2 ($F = 11.17$, $p = 0.0032$) terms were significant, confirming curvature in the dosage and initial concentration dimensions, while the A^2 term was not ($F = 1.49$, $p = 0.24$), so that pH acts approximately linearly on C_e within the studied range. The two nonsignificant terms were retained so that the ML models are compared with the full second-order polynomial.

The lack-of-fit test was significant (F = 20.94, p = 0.014), so the second-order polynomial should be regarded as an empirical approximation of the response surface rather than an exact representation. The four center-point replicates (C_e = 6.18, 7.20, 6.88, and 6.16 mg/L) give a pure-error SD of only 0.52 mg/L (MS_{PE} = 0.27), about 1.4% of the response range, so that the test detects even modest systematic deviations from the quadratic form. In addition, the two largest residuals (Run 3: +4.22 mg/L; Run 6: −6.17 mg/L) both occur at pH 2 with C_0 = 50 mg/L, where uptake approaches capacity limitation and the symmetric quadratic form is least flexible. The R^2 values should therefore be read as evidence of good average predictive ability within the design space rather than of uniform adequacy throughout it. Residual diagnostics are presented in Fig. S1 (Additional file 1). The normal probability plot deviates from the diagonal mainly at Runs 3 and 6, the residuals show no systematic curvature against the predicted values, and no data points were excluded from any analysis.

Table 3 Three-factor, three-level full factorial design matrix and the measured, predicted, and residual equilibrium RhB concentrations

Run	pH	Dosage (g/L)	C_0 (mg/L)	C_e measured (mg/L)	Removal (%)	C_e predicted (mg/L)	Residual (mg/L)
1	2	2	10	0.31	96.9	0.06	+0.25
2	2	2	30	3.51	88.3	6.51	−3.00
3	2	2	50	22.80	54.4	18.58	+4.22
4	2	5	10	0.15	98.5	−1.61	+1.76
5	2	5	30	0.54	98.2	0.21	+0.33
6	2	5	50	1.48	97.0	7.65	−6.17
7	2	8	10	0.04	99.6	0.54	−0.50
8	2	8	30	0.47	98.4	−2.26	+2.73
9	2	8	50	0.92	98.2	0.54	+0.38
10	4	2	10	1.75	82.5	3.22	−1.47
11	4	2	30	13.88	53.7	13.61	+0.27
12	4	2	50	31.17	37.7	29.61	+1.56
13	4	5	10	1.39	86.1	0.93	+0.46
14	4	5	30	6.18	79.4	6.69	−0.51
15	4	5	50	19.51	61.0	18.06	+1.45
16	4	8	10	0.55	94.5	2.47	−1.92
17	4	8	30	3.38	88.7	3.60	−0.22
18	4	8	50	10.55	78.9	10.33	+0.22
19	6	2	10	5.21	47.9	4.33	+0.88
20	6	2	30	18.26	39.1	18.65	−0.39
21	6	2	50	36.28	27.4	38.59	−2.31
22	6	5	10	2.55	74.5	1.43	+1.12
23	6	5	30	12.08	59.7	11.12	+0.96
24	6	5	50	26.85	46.3	26.42	+0.43
25	6	8	10	1.79	82.1	2.36	−0.57
26	6	8	30	7.07	76.4	7.41	−0.34
27	6	8	50	18.30	63.4	18.08	+0.22

Run	pH	Dosage (g/L)	C_0 (mg/L)	C_e measured (mg/L)	Removal (%)	C_e predicted (mg/L)	Residual (mg/L)
28	4	5	30	7.20	76.0	6.69	+0.51
29	4	5	30	6.88	77.1	6.69	+0.19
30	4	5	30	6.16	79.5	6.69	−0.53

Runs 14 and 28–30 are replicate experiments at the design center point (pH 4, dosage 5 g/L, C_0 = 30 mg/L). Predicted values and residuals were calculated from the fitted second-order polynomial model. Runs are listed in standard order.

Table 4 ANOVA for the quadratic RSM model (Type III SS)

Source	SS	df	MS	*F*	*p*-value	η^2	
Model	2845.52	9	316.17	65.38	<0.0001		*
A (pH)	535.41	1	535.41	110.72	<0.0001	0.182	*
B (Dosage)	451.00	1	451.00	93.26	<0.0001	0.153	*
C (C_0)	1319.61	1	1319.61	272.89	<0.0001	0.449	*
AB	4.56	1	4.56	0.94	0.3429	0.002	
AC	185.50	1	185.50	38.36	<0.0001	0.063	*
BC	257.52	1	257.52	53.25	<0.0001	0.087	*
A^2	7.20	1	7.20	1.49	0.2364	0.002	
B^2	25.10	1	25.10	5.19	0.0338	0.009	*
C^2	54.02	1	54.02	11.17	0.0032	0.018	*
Residual	96.72	20	4.84				
Lack of fit	95.91	17	5.64	20.94	0.0143		*
Pure error	0.81	3	0.27				
Total	2942.23	29					

R^2 = 0.9671, adj-R^2 = 0.9523, pred-R^2 = 0.9112, adequate precision = 32.18. * Significant at $p < 0.05$. SS = sum of squares; df = degrees of freedom; MS = mean square.

3.7.2. Response surface analysis

At C_0 = 30 mg/L (Fig. 3a), C_e is lowest at low pH and high dosage, in line with the negative coefficient of *B* (−5.01) and the positive coefficient of *A* (+5.45). At high dosage the contour lines turn toward the dosage axis, that is, further dosage lowers C_e only slightly once the adsorbent is in excess, a pattern captured by the significant B^2 term (p = 0.034).

At a dosage of 5 g/L (Fig. 3b), the surface is steepest along C_0, which has the largest main effect (+8.56) and interacts with pH (*AC*, +3.93). When C_0 was raised from 10 to 50 mg/L, the measured C_e rose from 0.15 to 1.48 mg/L at pH 2 but from 2.55 to 26.85 mg/L at pH 6 (Table 3). This interaction follows from the speciation of RhB acting on a surface of finite, pH-independent exchange capacity (Sections 3.4 to 3.6). At pH 2, RhB^+ has a high affinity for the external surface and its uptake is not yet limited by capacity, so most of an increase in C_0 is taken up by the solid. At pH 6, the zwitterionic form predominates and the additional dye remains largely in solution.

At pH 4 (Fig. 3c), the *BC* interaction is strong (−4.63, $p < 0.0001$). At C_0 = 10 mg/L, the fitted C_e was low at both dosage extremes (3.2 and 2.5 mg/L at 2 and 8 g/L, respectively), because the available sites

far exceeded the dye molecules. At C_0 = 50 mg/L, raising the dosage from 2 to 8 g/L reduced the fitted C_e from 29.6 to 10.3 mg/L, corresponding to removals of 41% and 79%. In practice, the dosage matters mainly for the more concentrated effluents.

Within the investigated design, removals above 97% were achieved at pH 2 with dosages of 5 g/L and above across the whole C_0 range (Runs 4 to 9, C_e from 0.04 to 1.48 mg/L). Minimization of the fitted polynomial over $[-1, +1]^3$ placed its minimum at pH 2 and 8 g/L; the slightly negative predictions at pH 2 in Table 3 arise from the unconstrained quadratic form. Because C_0 is an influent characteristic rather than an operational variable, the adjustable parameters are pH and dosage, for which the model favors low pH and high dosage. Since pH 2 lies on the design boundary and strongly acidic operation is of limited practical utility, the more relevant result is the removal measured at pH 4 with the highest dosage, 94.5%, 88.7%, and 78.9% at C_0 = 10, 30, and 50 mg/L (Runs 16 to 18).

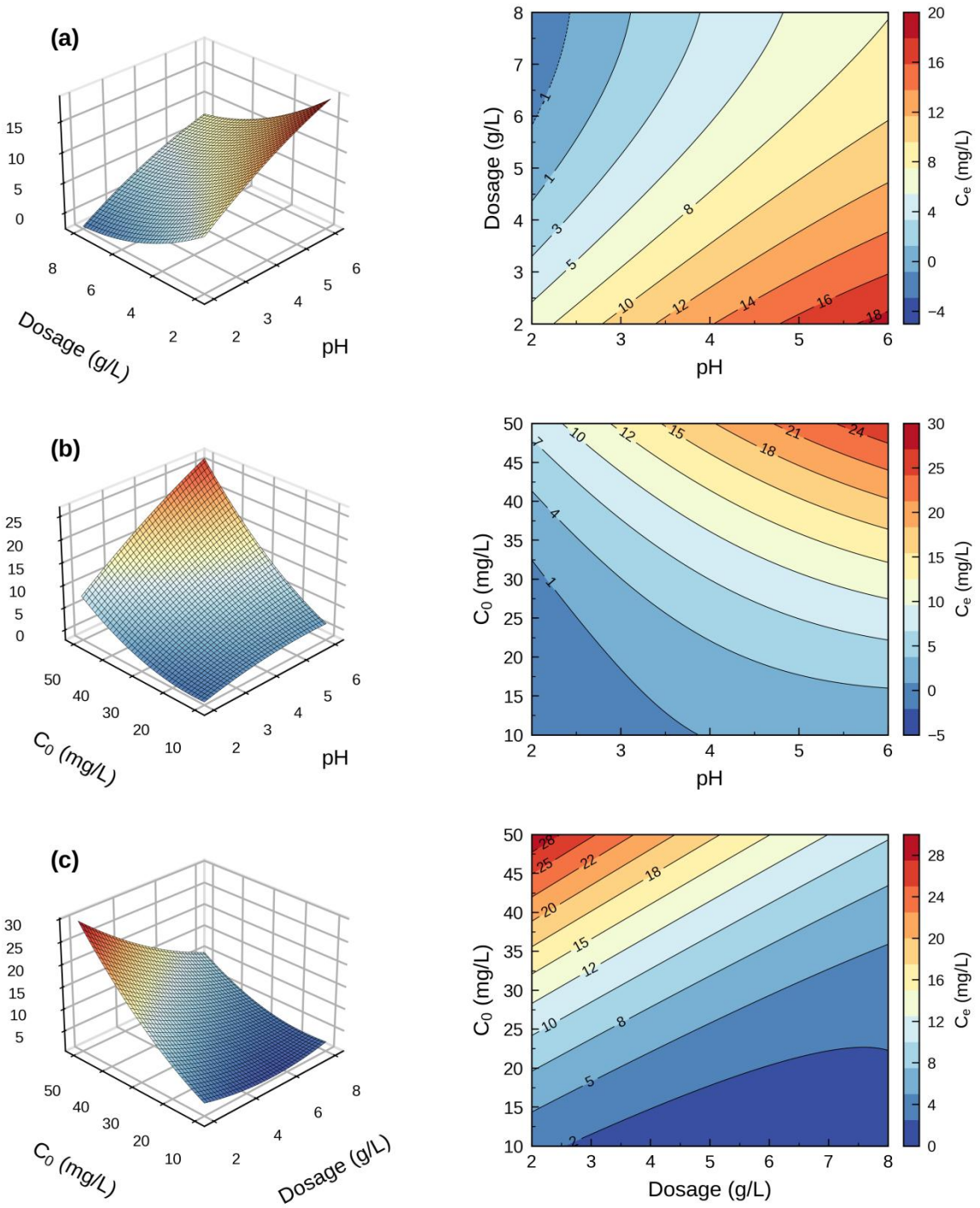

Fig. 3 Three-dimensional response surface plots and contour plots of C_e as a function of (a) pH and dosage at C_0 = 30 mg/L, (b) pH and C_0 at a dosage of 5 g/L, and (c) dosage and C_0 at pH 4

3.8. Machine learning prediction and SHAP analysis

3.8.1. Model performance comparison

Table 5 compares the predictive performance of the four models under LOOCV, together with the training R^2 of each model as an indicator of overfitting, and Fig. 4 shows the parity plots of the held-out predictions.

SVR achieved the highest LOOCV accuracy (R^2 = 0.925, RMSE = 2.72 mg/L, MAE = 1.64 mg/L), closely followed by RSM (R^2 = 0.911, RMSE = 2.95 mg/L, MAE = 1.91 mg/L); the difference between the two is small and not statistically significant (paired Wilcoxon signed-rank test on the absolute residuals, p = 0.28), whereas both models gave lower errors than XGBoost and RF. The selected SVR hyperparameters (C = 100, γ = 0.1, ε = 0.1) lie inside the search grid and not at its edges (Additional file 1: Table S5). The PRESS-based pred-R^2 of the quadratic model is numerically identical to its LOOCV R^2 (0.911), as expected for a linear model.

Because the ML hyperparameters were selected on the same LOOCV predictions used to score them, the ML entries in Table 5 are optimistic estimates, whereas RSM has no tunable hyperparameters. When the SVR grid search was repeated within each training fold (nested LOOCV), R^2 decreased to 0.858, below the RSM baseline, and RMSE increased to 3.73 mg/L (Wilcoxon p = 0.54). The apparent advantage of SVR over the quadratic model is therefore not robust to hyperparameter selection, and the two models are statistically indistinguishable on this dataset.

Adsorption studies that compare RSM with ML on designed datasets of similar size often report that ML is more accurate. [28,29] Part of the difference from the present result probably lies in how the models were validated. A single random split that keeps 70–80% of the observations for training leaves only 6–9 test points on a 30-observation dataset, so the accuracy estimate depends strongly on which points happen to be held out, and tuning the hyperparameters on those same points biases the ML metrics upward but not those of the quadratic model. LOOCV uses every observation once as the test point, and nesting the grid search inside it removes the tuning bias. With both safeguards in place, SVR no longer outperformed the quadratic model, so some of the ML advantage reported for small datasets may come from the evaluation protocol.

XGBoost yielded intermediate performance (LOOCV R^2 = 0.877, RMSE = 3.48 mg/L, MAE = 2.33 mg/L) and RF the lowest (R^2 = 0.755, RMSE = 4.90 mg/L, MAE = 3.57 mg/L). Both tree ensembles overfitted substantially: XGBoost reached a training R^2 of 0.9997 against a LOOCV R^2 of 0.877, and RF 0.971 against 0.755, whereas SVR (0.982 versus 0.925) and RSM (0.967 versus 0.911) maintained modest gaps owing to their built-in regularization: the ε-insensitive tube and kernel smoothness for SVR, and the parametric constraint of the quadratic form for RSM. With only 29 training observations per fold, the tree ensembles do not have enough data to learn splits that generalize, which agrees with the general finding that simple models outperform high-capacity ensembles when data are scarce. [39]

The parity plots (Fig. 4) visualize these differences: the SVR and RSM points cluster tightly around the diagonal across the full concentration range, XGBoost shows generally good agreement with several individual deviations, and RF exhibits markedly wider scatter, overpredicting the lowest concentrations and underpredicting those above 20 mg/L by 6–10 mg/L.

Table 5 Predictive performance of the RSM and ML models under leave-one-out cross-validation (LOOCV)

Model	Training R^2	LOOCV R^2	RMSE (mg/L)	MAE (mg/L)	Hyperparameters
RSM	0.9671	0.9112	2.95	1.91	Second-order polynomial
SVR	0.9817	0.9246	2.72	1.64	C = 100, γ = 0.1, ε = 0.1
SVR (nested LOOCV)	n/a	0.8581	3.73	2.16	re-selected within each fold
XGBoost	0.9997	0.8765	3.48	2.33	n = 200, depth = 4, lr = 0.1, ss = 0.7
RF	0.9713	0.7550	4.90	3.57	n = 100, depth = 7, leaf = 1

For the tuned ML models the LOOCV metrics involve hyperparameter optimization on the same folds and are therefore optimistic; the SVR (nested LOOCV) row provides the estimate free of the optimism introduced by hyperparameter selection, for which a training R^2 is not defined. SVR = support vector regression; RF = random forest. n = number of trees; depth = maximum tree depth; lr = learning rate; ss = subsample ratio; leaf = minimum number of samples per leaf; n/a = not applicable.

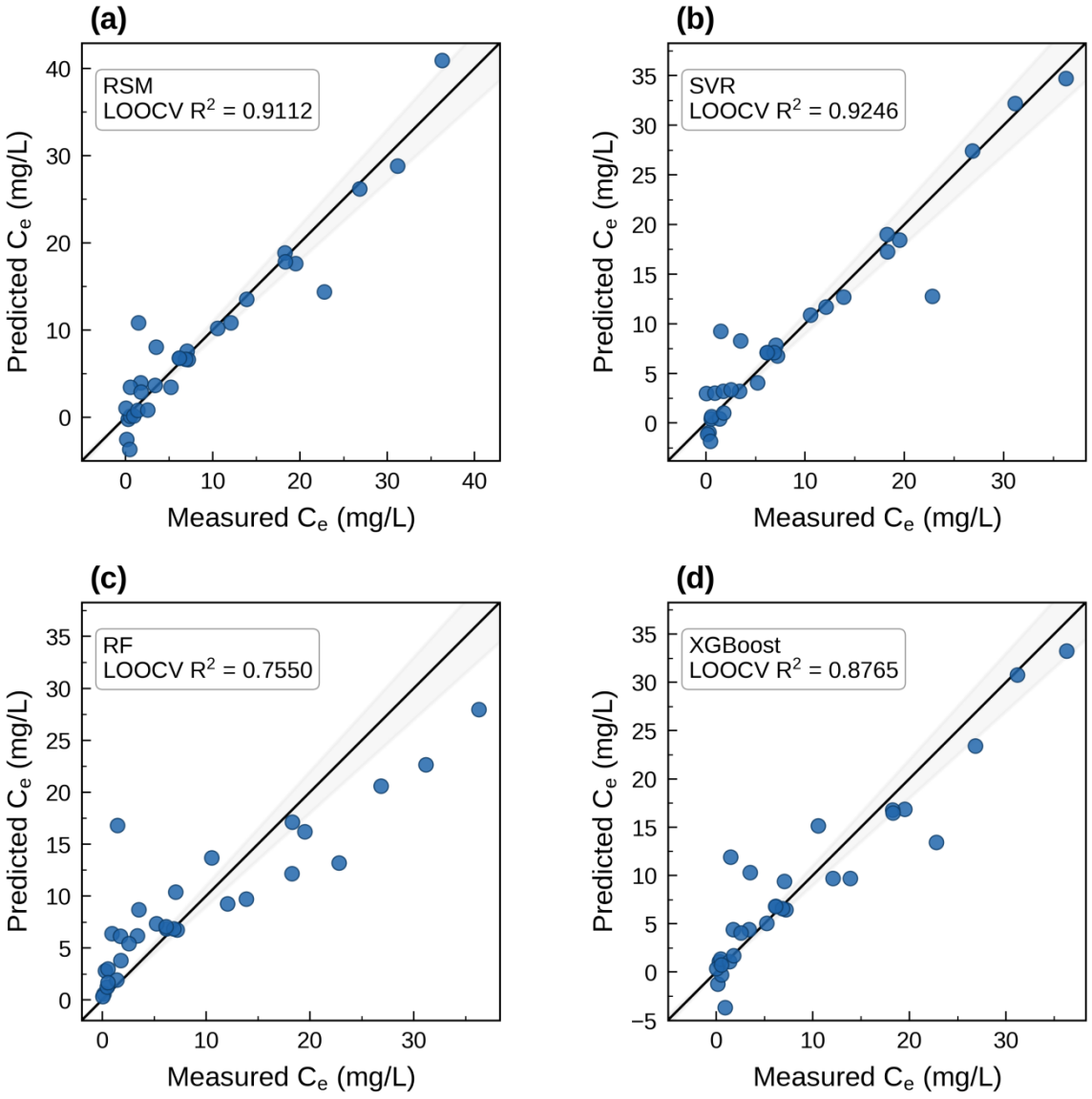

Fig. 4 Parity plots of LOOCV-predicted versus measured C_e values for (a) RSM, (b) SVR, (c) RF, and (d) XGBoost; the shaded band marks ±10% of the measured value

3.8.2. SHAP feature importance and dependence analysis

SHAP analysis was performed on all three ML models to evaluate the robustness of the feature importance ranking across learning algorithms (Fig. 5a), and the beeswarm and dependence plots of the SVR model (Fig. 5b, c) were used to examine the direction of each effect.

The ranking of global feature importance, quantified by mean |SHAP|, was identical across the three models: C_0 > pH > dosage. SVR gave mean |SHAP| values of 5.91, 3.39, and 3.28 mg/L for C_0, pH, and dosage, respectively, XGBoost closely comparable values (5.93, 3.54, 3.39), and RF proportionally lower magnitudes (5.56, 2.99, 2.96), consistent with its lower predictive accuracy. The convergence of

a kernel method, a bagging ensemble, and a boosting ensemble on the same hierarchy indicates that the ranking is a property of the dataset rather than of any single model, and it coincides with the ANOVA ordering of Table 4 (C_0: F = 272.89 > pH: F = 110.72 > dosage: F = 93.26). The dominance of C_0 is partly structural, because C_e is related to C_0 through the adsorption mass balance ($C_e = C_0 - q_e \cdot m/V$), so the mechanistically informative content of the SHAP analysis lies in the direction and consistency of the pH and dosage contributions.

The beeswarm plot (Fig. 5b) shows the direction and magnitude of each feature's influence on C_e. High C_0 values correspond to strongly positive SHAP values and low values to strongly negative ones, with the SHAP range for C_0 spanning from −11.2 to +13.4 mg/L. For pH, low values (pH 2) produce negative contributions (lower C_e, higher removal) and high values (pH 6) positive contributions, in the same direction as the single-factor pH trend of Section 3.4 and consistent with the speciation-dependent cation exchange mechanism discussed in Section 3.6. For dosage, high values yield negative SHAP values, reflecting the additional adsorption sites provided at higher adsorbent loading.

The dependence plots (Fig. 5c) resolve these effects by factor level. The pH contributions are uniformly negative at pH 2 (−3.1 to −8.2 mg/L, mean −5.6 mg/L) and uniformly positive at pH 6 (+2.9 to +6.9 mg/L, mean +5.0 mg/L). Within each pH level, higher C_0 values shift the contribution upward, visualizing the pH × C_0 interaction identified in the ANOVA (F = 38.36). The dosage plot shows a monotonically decreasing trend whose magnitude is larger at high C_0, corresponding to the dosage × C_0 interaction (F = 53.25). The C_0 plot shows a strongly positive, nearly monotonic relationship in which low dosage amplifies the positive contributions, that is, insufficient adsorbent at high C_0 gives the largest residual concentrations. The SHAP analysis thus reproduces the ranking of the effects, the direction of the single-factor trends, and the two significant interactions found in the designed experiment.

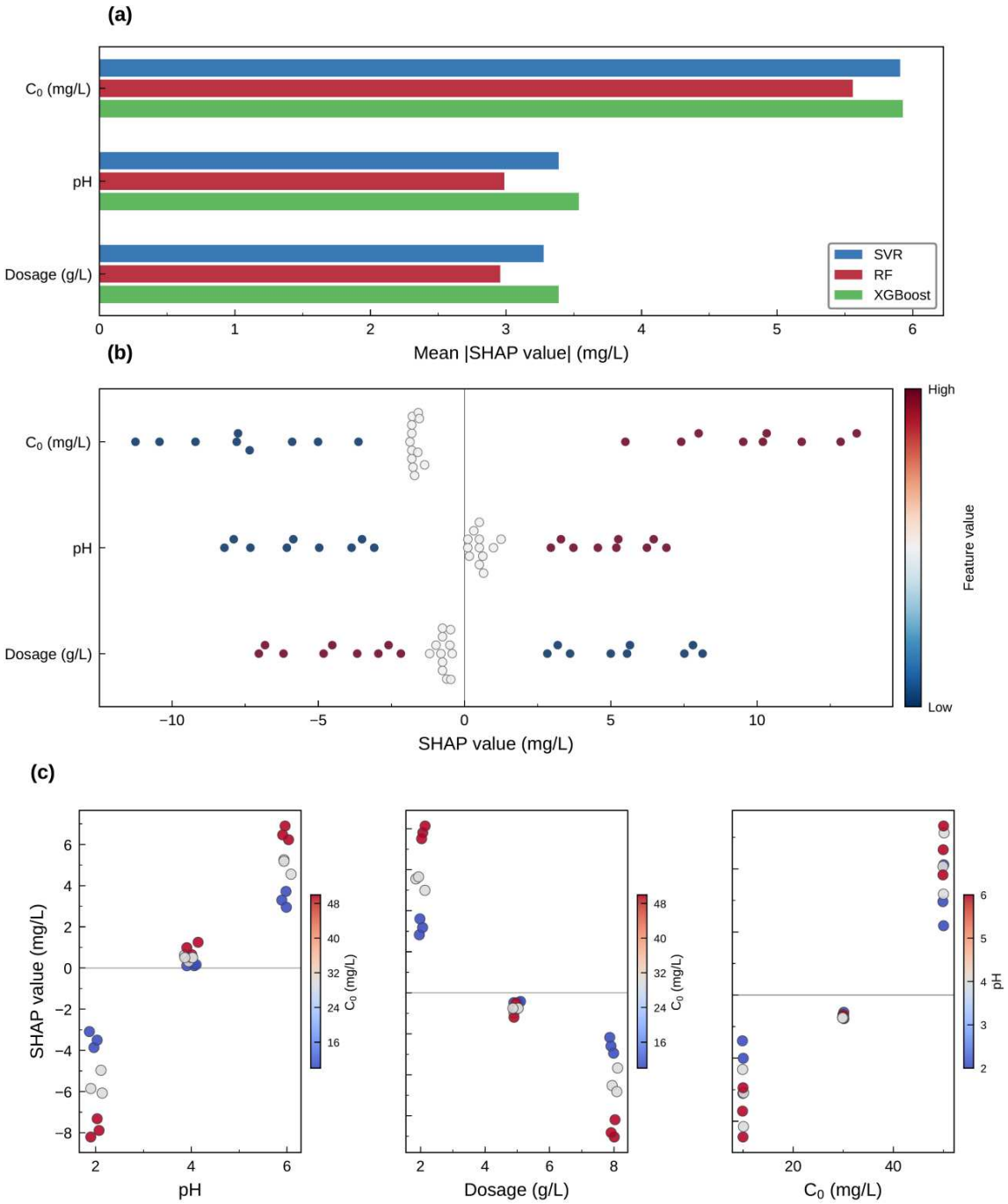

Fig. 5 SHAP analysis of the ML models: (a) comparison of mean |SHAP value| feature importance across SVR, RF, and XGBoost, (b) beeswarm plot of SHAP values for the SVR model, and (c) dependence plots for pH, dosage, and C_0 (SVR)

3.9. Limitations

This work was carried out with single-solute RhB solutions in deionized water, in batch mode, and at a single temperature (25 ± 2 °C). Competing cations and natural organic matter in real effluents, the

regeneration of the spent zeolite, fixed-bed operation, and the thermodynamics of the uptake were outside its scope. The cation exchange contribution was inferred from the pH dependence, the speciation of RhB, and the surface coverage, and its direct confirmation through the release of exchangeable cations is left for future work. The model comparison applies to small designed datasets of this type and should not be extrapolated to larger or space-filling datasets.

4. Conclusions

Unmodified natural zeolite removed RhB effectively under acidic conditions, with 98.0% removal at pH 2 and a Langmuir capacity of 6.60 mg/g at pH 6. The adsorbent was identified by XRD as mordenite with quartz as the main accompanying mineral; its mean Si/Al ratio from EDX was 5.58, its BET surface area 26.6 m^2/g, and its external surface area 8.81 m^2/g. Five observations are consistent with an external-surface mechanism: the strong pH dependence that follows RhB speciation, the permanently negative framework charge, the exclusion of RhB from the mordenite channels, the small fraction of the CEC used, and a coverage on the order of one dye layer on the external surface at pH 6. In this mechanism, ion exchange of the cationic form accounts for the pH-sensitive part of the uptake, and a comparable pH-insensitive component persists into the zwitterionic regime. The quadratic RSM model described the 30-run full factorial dataset with R^2 = 0.967 and pred-R^2 = 0.911, and removals above 97% were obtained at pH 2 with dosages of 5 g/L and above across the whole concentration range. Under LOOCV, SVR gave the highest apparent accuracy (R^2 = 0.925), but nested LOOCV, which removes the optimistic bias of in-sample hyperparameter tuning, reduced this to 0.858, so that SVR and the quadratic model are statistically indistinguishable on this dataset (Wilcoxon p = 0.54) while both gave lower errors than the tree ensembles; the more complex models did not generalize better. SHAP analysis reproduced the ANOVA effect hierarchy (C_0 > pH > dosage) and the direction of the single-factor trends in all three ML models. Because the highest removal requires pH 2, the most plausible application is intrinsically acidic dye-bearing streams. For designed adsorption datasets of this size, the quadratic model is therefore a sound first choice for prediction, and ML with SHAP is better used to check it than to replace it.

List of abbreviations and symbols

Symbol	Description	Unit
Roman symbols		
A	Absorbance at 554 nm	–
A, B, C	Coded levels of pH, adsorbent dosage, and C_0, respectively (Section 2.4)	–
C	Constant related to boundary-layer thickness (Weber-Morris model)	mg/g
C (SVR)	Regularization parameter of support vector regression	–
C_0	Initial RhB concentration	mg/L
C_e	Equilibrium RhB concentration	mg/L
f_{cat}	Mole fraction of cationic RhB	–
F	Fisher test statistic	–
k_1	Pseudo-first-order rate constant	min^{-1}
k_2	Pseudo-second-order rate constant	g/(mg·min)
k_{id}	Intraparticle diffusion rate constant	$mg/(g \cdot min^{0.5})$
K_F	Freundlich capacity constant	$(mg/g)(L/mg)^{1/n}$
K_L	Langmuir affinity constant	L/mg
K_S	Sips affinity constant	L/mg
m	Mass of adsorbent	g
m_S	Sips heterogeneity exponent	–
$1/n$	Freundlich heterogeneity parameter	–
p	Probability value of a significance test	–
$p/p°$	Relative pressure in N_2 physisorption	–
q_{cat}	Uptake of the cationic form	mg/g
q_e	Equilibrium adsorption capacity	mg/g
q_{max}	Maximum monolayer adsorption capacity	mg/g
q_t	Amount adsorbed at time t	mg/g
q_{zwitt}	Uptake of the zwitterionic form	mg/g
R^2	Coefficient of determination	–
t	Contact time	min
V	Volume of solution	L
Greek symbols		
γ	Kernel coefficient of the radial basis function kernel in SVR	–
ε	Width of the epsilon-insensitive tube in SVR	–
η^2	Eta squared (effect size), effect SS / total SS	–
λ	Wavelength of Cu Kα radiation	Å
Abbreviations		
ANOVA	Analysis of variance	
BET	Brunauer-Emmett-Teller	
BJH	Barrett-Joyner-Halenda	
CEC	Cation exchange capacity	
FTIR	Fourier transform infrared spectroscopy	
LOOCV	Leave-one-out cross-validation	
MAE	Mean absolute error	
ML	Machine learning	
MS_{PE}	Mean square of pure error	
PFO	Pseudo-first-order	
PRESS	Prediction error sum of squares	
PSO	Pseudo-second-order	
RF	Random forest	
RhB	Rhodamine B	

Symbol	Description	Unit
RMSE	Root mean square error	
RSM	Response surface methodology	
SD	Standard deviation	
SEM-EDX	Scanning electron microscopy with energy-dispersive X-ray spectroscopy	
SHAP	SHapley Additive exPlanations	
SVR	Support vector regression	
XGBoost	Extreme gradient boosting	
XRD	X-ray diffraction	

Declarations

Ethics approval and consent to participate

Not applicable.

Consent for publication

Not applicable.

Availability of data and materials

The adsorption data generated or analyzed during this study and the Python script used for the response surface, machine learning, and SHAP analyses are included in this published article and its additional file (Additional file 1). The raw characterization data (XRD pattern, N_2 physisorption isotherm, FTIR spectra, EDX spectra, and SEM images) are available from the corresponding author on reasonable request.

Competing interests

The authors declare that they have no competing interests.

Funding

No funding was received for this study.

Authors' contributions

WY designed the methodology, carried out the experiments, wrote the analysis code, analyzed the data, prepared the figures, and wrote the original draft. RA conceived and supervised the study, curated the data, and reviewed and edited the manuscript. All authors read and approved the final manuscript.

Acknowledgements

The authors thank the School of Civil Engineering, Universiti Sains Malaysia, for providing the laboratory facilities used in this work.

References

[1] V.K. Gupta, Suhas, Application of low-cost adsorbents for dye removal – A review, J. Environ. Manage. 90 (2009) 2313–2342. https://doi.org/10.1016/j.jenvman.2008.11.017.

[2] M.T. Yagub, T.K. Sen, S. Afroze, H.M. Ang, Dye and its removal from aqueous solution by adsorption: A review, Adv. Colloid Interface Sci. 209 (2014) 172–184. https://doi.org/10.1016/j.cis.2014.04.002.

[3] A.K. Verma, R.R. Dash, P. Bhunia, A review on chemical coagulation/flocculation technologies for removal of colour from textile wastewaters, J. Environ. Manage. 93 (2012) 154–168. https://doi.org/10.1016/j.jenvman.2011.09.012.

[4] K. Hunger (Ed.), Industrial Dyes: Chemistry, Properties, Applications, Wiley-VCH, Weinheim, 2003. https://doi.org/10.1002/3527602011.

[5] G. Crini, Non-conventional low-cost adsorbents for dye removal: A review, Bioresour. Technol. 97 (2006) 1061–1085. https://doi.org/10.1016/j.biortech.2005.05.001.

[6] A. Dąbrowski, Adsorption — from theory to practice, Adv. Colloid Interface Sci. 93 (2001) 135–224. https://doi.org/10.1016/S0001-8686(00)00082-8.

[7] S. Wang, Y. Peng, Natural zeolites as effective adsorbents in water and wastewater treatment, Chem. Eng. J. 156 (2010) 11–24. https://doi.org/10.1016/j.cej.2009.10.029.

[8] M.W. Ackley, S.U. Rege, H. Saxena, Application of natural zeolites in the purification and separation of gases, Microporous Mesoporous Mater. 61 (2003) 25–42. https://doi.org/10.1016/S1387-1811(03)00353-6.

[9] A. Hedström, Ion exchange of ammonium in zeolites: A literature review, J. Environ. Eng. 127 (2001) 673–681. https://doi.org/10.1061/(ASCE)0733-9372(2001)127:8(673).

[10] I. Rodríguez-Iznaga, M.G. Shelyapina, V. Petranovskii, Ion exchange in natural clinoptilolite: Aspects related to its structure and applications, Minerals 12 (2022) 1628. https://doi.org/10.3390/min12121628.

[11] A. Ateş, G. Akgül, Modification of natural zeolite with NaOH for removal of manganese in drinking water, Powder Technol. 287 (2016) 285–291. https://doi.org/10.1016/j.powtec.2015.10.021.

[12] V. Meshko, L. Markovska, M. Mincheva, A.E. Rodrigues, Adsorption of basic dyes on granular activated carbon and natural zeolite, Water Res. 35 (2001) 3357–3366. https://doi.org/10.1016/S0043-1354(01)00056-2.

[13] S. Wang, Z. Zhu, Characterisation and environmental application of an Australian natural zeolite for basic dye removal from aqueous solution, J. Hazard. Mater. 136 (2006) 946–952. https://doi.org/10.1016/j.jhazmat.2006.01.038.

[14] D. Karadag, E. Akgul, S. Tok, F. Erturk, M.A. Kaya, M. Turan, Basic and reactive dye removal using natural and modified zeolites, J. Chem. Eng. Data 52 (2007) 2436–2441. https://doi.org/10.1021/je7003726.

[15] X. Jin, M.-Q. Jiang, X.-Q. Shan, Z.-G. Pei, Z. Chen, Adsorption of methylene blue and orange II onto unmodified and surfactant-modified zeolite, J. Colloid Interface Sci. 328 (2008) 243–247. https://doi.org/10.1016/j.jcis.2008.08.066.

[16] A. Badeenezhad, A. Azhdarpoor, S. Bahrami, S. Yousefinejad, Removal of methylene blue dye from aqueous solutions by natural clinoptilolite and clinoptilolite modified by iron oxide nanoparticles, Mol. Simul. 45 (2019) 564–571. https://doi.org/10.1080/08927022.2018.1564077.

[17] R.H. Myers, D.C. Montgomery, C.M. Anderson-Cook, Response Surface Methodology: Process and Product Optimization Using Designed Experiments, 4th ed., Wiley, Hoboken, NJ, 2016.

[18] D. Baş, İ.H. Boyacı, Modeling and optimization I: Usability of response surface methodology, J. Food Eng. 78 (2007) 836–845. https://doi.org/10.1016/j.jfoodeng.2005.11.024.

[19] B. Ghattas, D. Manzon, Machine learning alternatives to response surface models, Mathematics 11 (2023) 3406. https://doi.org/10.3390/math11153406.

[20] L. Breiman, Random forests, Mach. Learn. 45 (2001) 5–32. https://doi.org/10.1023/A:1010933404324.

[21] V.N. Vapnik, The Nature of Statistical Learning Theory, 2nd ed., Springer, New York, 2000. https://doi.org/10.1007/978-1-4757-3264-1.

[22] T. Chen, C. Guestrin, XGBoost: A scalable tree boosting system, in: Proceedings of the 22nd ACM SIGKDD International Conference on Knowledge Discovery and Data Mining, ACM, New York, 2016, pp. 785–794. https://doi.org/10.1145/2939672.2939785.

[23] A. Mosavi, M. Salimi, S. Faizollahzadeh Ardabili, T. Rabczuk, S. Shamshirband, A.R. Varkonyi-Koczy, State of the art of machine learning models in energy systems, a systematic review, Energies 12 (2019) 1301. https://doi.org/10.3390/en12071301.

[24] S. Zhu, S. Heddam, E.K. Nyarko, M. Hadzima-Nyarko, S. Piccolroaz, S. Wu, Modeling daily water temperature for rivers: comparison between adaptive neuro-fuzzy inference systems and artificial neural networks models, Environ. Sci. Pollut. Res. 26 (2019) 402–420. https://doi.org/10.1007/s11356-018-3650-2.

[25] Z.H. Jaffari, H. Jeong, J. Shin, J. Kwak, C. Son, Y.-G. Lee, S. Kim, K. Chon, K.H. Cho, Machine-learning-based prediction and optimization of emerging contaminants' adsorption capacity on biochar materials, Chem. Eng. J. 466 (2023) 143073. https://doi.org/10.1016/j.cej.2023.143073.

[26] S. Moosavi, O. Manta, Y.A. El-Badry, E.E. Hussein, Z.M. El-Bahy, N.F.B. Mohd Fawzi, J. Urbonavičius, S.M.H. Moosavi, A study on machine learning methods' application for dye adsorption prediction onto agricultural waste activated carbon, Nanomaterials 11 (2021) 2734. https://doi.org/10.3390/nano11102734.

[27] O. Kulkarni, P. Dongare, B. Shanmughan, A. Nighojkar, S. Pandey, B. Kandasubramanian, Machine learning-assisted prediction of engineered carbon systems' capacity to treat textile dyeing wastewater via adsorption technology, Environ. Monit. Assess. 197 (2025) 223. https://doi.org/10.1007/s10661-025-13664-9.

[28] C.E. Onu, J.T. Nwabanne, P.E. Ohale, C.O. Asadu, Comparative analysis of RSM, ANN and ANFIS and the mechanistic modeling in eriochrome black-T dye adsorption using modified clay, S. Afr. J. Chem. Eng. 36 (2021) 24–42. https://doi.org/10.1016/j.sajce.2020.12.003.

[29] S. Kumari, S. Agarwal, M. Kumar, P. Sharma, A. Kumar, A. Hashem, N.H. Alotaibi, E.F. Abd-Allah, M.C. Garg, An exploration of RSM, ANN, and ANFIS models for methylene blue dye adsorption using Oryza sativa straw biomass: a comparative approach, Sci. Rep. 15 (2025) 2979. https://doi.org/10.1038/s41598-025-87274-3.

[30] S.M. Lundberg, S.-I. Lee, A unified approach to interpreting model predictions, in: Advances in Neural Information Processing Systems 30, Curran Associates, Red Hook, NY, 2017, pp. 4765–4774.

[31] S. Lagergren, Zur Theorie der sogenannten Adsorption gelöster Stoffe, K. Sven. Vetenskapsakad. Handl. 24 (1898) 1–39.

[32] Y.S. Ho, G. McKay, Pseudo-second order model for sorption processes, Process Biochem. 34 (1999) 451–465. https://doi.org/10.1016/S0032-9592(98)00112-5.

[33] W.J. Weber, J.C. Morris, Kinetics of adsorption on carbon from solution, J. Sanit. Eng. Div. Am. Soc. Civ. Eng. 89 (1963) 31–59. https://doi.org/10.1061/JSEDAI.0000430.

[34] I. Langmuir, The adsorption of gases on plane surfaces of glass, mica and platinum, J. Am. Chem. Soc. 40 (1918) 1361–1403. https://doi.org/10.1021/ja02242a004.

[35] H. Freundlich, Über die Adsorption in Lösungen, Z. Phys. Chem. 57 (1907) 385–470. https://doi.org/10.1515/zpch-1907-5723.

[36] R. Sips, On the structure of a catalyst surface, J. Chem. Phys. 16 (1948) 490–495. https://doi.org/10.1063/1.1746922.

[37] D.C. Montgomery, Design and Analysis of Experiments, 10th ed., Wiley, Hoboken, NJ, 2020.

[38] R. Kohavi, A study of cross-validation and bootstrap for accuracy estimation and model selection, in: Proceedings of the 14th International Joint Conference on Artificial Intelligence, Vol. 2, Morgan Kaufmann, San Francisco, CA, 1995, pp. 1137–1143.

[39] T. Hastie, R. Tibshirani, J. Friedman, The Elements of Statistical Learning, 2nd ed., Springer, New York, 2009. https://doi.org/10.1007/978-0-387-84858-7.

[40] S. Varma, R. Simon, Bias in error estimation when using cross-validation for model selection, BMC Bioinformatics 7 (2006) 91. https://doi.org/10.1186/1471-2105-7-91.

[41] G.C. Cawley, N.L.C. Talbot, On over-fitting in model selection and subsequent selection bias in performance evaluation, J. Mach. Learn. Res. 11 (2010) 2079–2107.

[42] Ch. Baerlocher, L.B. McCusker, D.H. Olson, Atlas of Zeolite Framework Types, 6th ed., Elsevier, Amsterdam, 2007. https://doi.org/10.1016/B978-0-444-53064-6.X5186-X.

[43] E. Passaglia, R.A. Sheppard, The crystal chemistry of zeolites, Rev. Mineral. Geochem. 45 (2001) 69–116. https://doi.org/10.2138/rmg.2001.45.2.

[44] M. Thommes, K. Kaneko, A.V. Neimark, J.P. Olivier, F. Rodriguez-Reinoso, J. Rouquerol, K.S.W. Sing, Physisorption of gases, with special reference to the evaluation of surface area and pore size distribution (IUPAC Technical Report), Pure Appl. Chem. 87 (2015) 1051–1069. https://doi.org/10.1515/pac-2014-1117.

[45] O. Korkuna, R. Leboda, J. Skubiszewska-Zięba, T. Vrublevs'ka, V.M. Gun'ko, J. Ryczkowski, Structural and physicochemical properties of natural zeolites: clinoptilolite and mordenite, Microporous Mesoporous Mater. 87 (2006) 243–254. https://doi.org/10.1016/j.micromeso.2005.08.002.

[46] H.N. Tran, S.-J. You, A. Hosseini-Bandegharaei, H.-P. Chao, Mistakes and inconsistencies regarding adsorption of contaminants from aqueous solutions: A critical review, Water Res. 120 (2017) 88–116. https://doi.org/10.1016/j.watres.2017.04.014.

[47] F. López Arbeloa, P. Ruiz Ojeda, I. López Arbeloa, Fluorescence self-quenching of the molecular forms of Rhodamine B in aqueous and ethanolic solutions, J. Lumin. 44 (1989) 105–112. https://doi.org/10.1016/0022-2313(89)90027-6.

[48] B. Ersoy, M.S. Çelik, Electrokinetic properties of clinoptilolite with mono- and multivalent electrolytes, Microporous Mesoporous Mater. 55 (2002) 305–312. https://doi.org/10.1016/S1387-1811(02)00433-X.

[49] A. Özkan, A.G. Şener, H. Üçbeyiay, Investigation of coagulation and electrokinetic behaviors of clinoptilolite suspension with multivalent cations, Sep. Sci. Technol. 53 (2018) 823–832. https://doi.org/10.1080/01496395.2017.1380669.

[50] J. Cieśla, W. Franus, M. Franus, K. Kedziora, J. Gluszczyk, J. Szerement, G. Jozefaciuk, Environmental-friendly modifications of zeolite to increase its sorption and anion exchange properties, physicochemical studies of the modified materials, Materials 12 (2019) 3213. https://doi.org/10.3390/ma12193213.

[51] K.Y. Foo, B.H. Hameed, Insights into the modeling of adsorption isotherm systems, Chem. Eng. J. 156 (2010) 2–10. https://doi.org/10.1016/j.cej.2009.09.013.

[52] K. Kuśmierek, J. Fronczyk, A. Świątkowski, Adsorptive removal of rhodamine B dye from aqueous solutions using mineral materials as low-cost adsorbents, Water Air Soil Pollut. 234 (2023) 531. https://doi.org/10.1007/s11270-023-06511-5.

[53] C. Tsamo, G.D. Kidwang, D.C. Dahaina, Removal of Rhodamine B from aqueous solution using silica extracted from rice husk, SN Appl. Sci. 2 (2020) 256. https://doi.org/10.1007/s42452-020-2057-0.

[54] W.-Y. Cheng, N. Li, Y.-Z. Pan, L.-H. Jin, The adsorption of rhodamine B in water by modified zeolites, Mod. Appl. Sci. 10 (2016) 67–76. https://doi.org/10.5539/mas.v10n5p67.

[55] A.A. AbdulRazak, S. Rohani, Sodium dodecyl sulfate-modified Fe_2O_3/molecular sieves for removal of rhodamine B dyes, Adv. Mater. Sci. Eng. 2018 (2018) 3849867. https://doi.org/10.1155/2018/3849867.

[56] A. Iryani, H. Nur, M. Santoso, D. Hartanto, Adsorption study of rhodamine B and methylene blue dyes with ZSM-5 directly synthesized from Bangka kaolin without organic template, Indones. J. Chem. 20 (2020) 130–140. https://doi.org/10.22146/ijc.41369.

[57] A.A. Oyekanmi, A. Ahmad, K. Hossain, M. Rafatullah, Adsorption of Rhodamine B dye from aqueous solution onto acid treated banana peel: Response surface methodology, kinetics and isotherm studies, PLoS One 14 (2019) e0216878. https://doi.org/10.1371/journal.pone.0216878.

[58] H. He, K. Chai, T. Wu, Z. Qiu, S. Wang, J. Hong, Adsorption of rhodamine B from simulated waste water onto kaolin-bentonite composites, Materials 15 (2022) 4058. https://doi.org/10.3390/ma15124058.

[59] Y.N. Kanafin, A. Mukhametrakhimova, R. Turpanova, S.G. Poulopoulos, Sustainable adsorption of rhodamine B and heavy metals using sewage sludge-derived biochar, ChemEngineering 10 (2026) 11. https://doi.org/10.3390/chemengineering10010011.

[60] G.B. Balji, P. Senthil Kumar, Sulphuric acid-modified coal fly ash for the removal of rhodamine B dye from water environment: Isotherm, kinetics, and thermodynamic studies, Adsorpt. Sci. Technol. 2023 (2023) 2808794. https://doi.org/10.1155/2023/2808794.

Additional files

Additional file 1: Supplementary Material. Table S1. Kinetic data for RhB adsorption onto natural zeolite. Table S2. Effect of adsorbent dosage. Table S3. Effect of initial solution pH. Table S4. Equilibrium isotherm data. Table S5. Hyperparameter grids searched for the three ML models. Fig. S1. Residual diagnostic plots for the quadratic RSM model. Supplementary Code. Python script used for the response surface, machine learning, and SHAP analyses.

Supplementary Files

This is a list of supplementary files associated with this preprint. Click to download.

- Additionalfile.docx